Electron Microscope Observations of Lattice Imperfections and Their Movement on the Atomic Scale

By H. Hashimoto

Okayama University of Science, 1-1 Ridai-cho, Okayama 700, Japan

Y. Takai

TDK Research Laboratory, 15-7 Higashi Ohwada 2, Ichikawa, Chiba 272-01, Japan

and Y. Yokota

Okayama University of Science, 1-1 Ridai-cho, Okayama 700, Japan

Abstract

The effect of partial coherence of illuminating electron waves on the image contrast is discussed. It is shown that aberration-free focus (AFF) imaging in axial and symmetrical illumination, which is generally believed to be the best imaging condition for coherent illumination, produces an inherent contrast which does not correspond to the atomic structure of the specimen. However, tilted-illumination AFF imaging produces the correct image. Atomic structure images of gold crystals containing edge, screw and mixed dislocations have been photographed, with tilted-illumination AFF imaging and by adjusting the specimen thickness to the optimum value, and the atomic structure of the core of these dislocations is discussed. The movement of these dislocations has been recorded on an atomic scale using a TV system, and the movement of atom columns accompanying the movement of dislocations is analyzed.

1. Introduction

Direct image recording of the movement of atom columns in crystals by a TV camera fastened to a transmission electron microscope was first carried out by the present authors (Hashimoto, Sugimoto, Takai & Endoh, 1978; Hashimoto, Yokota, Takai, Endoh & Kumao, 1978/79; Hashimoto, Takai, Yokota, Kumao, Endoh, Fukada & Tomioka, 1979; Hashimoto, Endoh, Takai, Yokota & Kumao, 1980; Hashimoto, Takai, Yokota, Endoh & Fukada, 1980). Since the intensity maxima or minima of the images of atoms in crystals do not always appear at the true positions of the atoms in the crystal, even when the illuminating beam is incident parallel to a symmetrical axis (Hashimoto, Endoh, Takai, Tomioka & Yokota, 1978/79) it is well understood that the theoretical image contrast calculation using the

dynamical theory of electron diffraction (Cowley & Moodie, 1957; Bethe, 1928; Howie & Whelan, 1961) and image formation theory has to be carried out and compared with the observed images. However, images of atoms in gold specimens whose thickness is adjusted to the optimum value so that the phases of all the image-forming diffracted waves are the same have been photographed by adjusting the lens to the aberration-free focus (AFF) imaging condition in tilted illumination (Takai, Hashimoto & Endoh, 1983). This method of observation produces the intensity maximum of the images at the correct position in the perfect crystal. This method has also been applied not only to perfect crystals but also to crystals containing a twin boundary and a stacking fault. The observed contrast was compared with theoretical images calculated by using Howie & Whelan (1962) many-beam diffraction and image formation theories considering the phase contrast transfer function and it was noted that the AFF imaging condition in tilted illumination produces images of the atoms in their correct position, with a resolution higher than the theoretical resolution limit for normal operation of the electron microscope.

Direct image recording by a movie camera in real time was carried out in 1957 (Whelan, Hirsch, Horn & Bollman, 1957) and in 1958 (Hashimoto, Tanaka, Kobayashi, Shimazu, Naiki & Mannami, 1958) and by TV camera in 1970 (Hashimoto, Kumao, Etoh, Fujiwara & Maeda, 1970; Imura, Saka & Yukawa, 1970). Image recording by TV camera on the atomic scale was first carried out by observing the crystal lattice fringe growth of γ-tungsten oxide (lattice fringe with 1·2 nm spacings) in 1970 (Hashimoto, Kumao, Etoh, Fujiwara & Maeda, 1970) and atomic lattice growing of ThO_2 small crystals by the decomposition of thorium pyromeritate in 1976 (Hashimoto, 1976) and in 1978 (Hashimoto, Kumao & Endoh, 1978) using a 100 kV conventional transmission electron microscope. It was noted in these

observations that atoms and their clusters change their position in each frame of the TV screen (interval is 0·03 s), which is very different from the observations by a scanning transmission electron microscope (Isaacson, 1976; Crewe, 1978) indicating that uranium atoms move 3 nm during 30 min (each frame was recorded with an interval of 40 s and very little movement was noted). A real-time image recording technique by a TV camera on the atomic scale was also applied to the Cambridge 600 keV electron microscope (Cosslett, 1977; Catto, Smith, Nixson, Erasmus & Smith, 1981) and the movements of CdTe pair atomic columns (Sinclair, Ponce, Yamashita, Smith, Camps, Freeman, Erasmus, Nixson, Smith & Catto, 1982), gold and silver atomic columns at their edges (Marks & Smith, 1983) were observed. TV recording systems on the atomic scale became more popular after they were commercialized and many interesting behaviors of atomic columns were reported (Bovin, Wallenburg & Smith, 1985; Iijima & Ichihashi, 1985).

In the present paper we show that the AFF tilt illumination is useful for eliminating the effect of partial coherence of the illuminating electron beam. Atomic structure images of an edge dislocation, a screw dislocation and a mixed dislocation which were recorded using tilted-illumination AFF imaging condition are analyzed; the movement of atoms accompanied by the movement of these imperfections have also been shown by recording on a TV system and movie film.

2. Effect of partial coherence of electron waves on tilted- and axial-illumination AFF

Atomic structure images of crystals are formed by interference not only between the transmitted primary wave and the diffracted waves but also among the diffracted waves. When the illuminating electron waves and the diffracted waves are not completely coherent, the effect of partial coherence of the image-forming waves has to be taken into account for the interpretation of the image contrast (O'Keefe, 1979; Ishizuka, 1980). Petal- and horseshoe-shaped image contrast in atoms appearing in [001] gold crystals at a deviated Bragg reflecting condition have been attributed to the partial coherence of the diffracted waves (Takai, Hashimoto, Endoh & Ajika, 1981; Hashimoto & Takai, 1985). At the present stage of electron microscopy, the image-forming electron waves are partially coherent. Thus it is important to adopt an imaging method without any effect of partial coherence in order to obtain images of atoms in their correct position with correct contrast. In our previous paper (Takai et al., 1983), the defocus and thickness dependence of the position of the intensity maxima of electron waves at the bottom face of a gold crystal in the [110] orientation are discussed.

In Fig. 1, the coherence dependence of the image contrast under axial illumination and tilted illumination is shown for three imaging cases using three waves (000, 1$\bar{1}$1 and $\bar{1}$$\bar{1}$1), four waves (000, 200, 1$\bar{1}$1 and 11$\bar{1}$) and seven waves (000, 200, $\bar{2}$00, 1$\bar{1}$1, $\bar{1}$$\bar{1}$1, 11$\bar{1}$ and $\bar{1}$1$\bar{1}$) in tilted- and axial-illumination AFF conditions. The calculation is based on the Howie-Whelan many-beam diffraction theory and image formation theory, considering spatial and temporal coherence of electron waves.

As can be seen in Figs. 1(a)-(d) and (a')-(d') in tilted-illumination AFF imaging, bright spot contrast appears at the correct atom position even if the order of partial coherence is increased. However as can be seen in Figs. 1(a'')-(d'') in axial-illumination AFF imaging, inherent extra bright spots appear at the position with no atoms. Therefore, though axial illumination has been recommended so far to obtain images of atoms at their correct position (Miyake, Fujiwara, Tokonami & Fujimoto, 1964), it does not give the correct image when partial coherence cannot be disregarded. This is because the coherence between the transmitted primary wave (000) and diffracted waves becomes small, and only the interference between the diffracted waves become predominant. Therefore, in the following observation of atom columns around the defects in the crystals, the tilted-illumination AFF imaging shown in Figs. 1(a')-(e') is used. In this case the angle of the 000 and 200 reflections against the optical axis α_1 is different from that of 1$\bar{1}$1 and 11$\bar{1}$, α_2. When the defocus Δf is $1/2C_s(\alpha_1^2 + \alpha_2^2) = 865$ Å the phase angles γ_g, given by $\pi/2\lambda(C_s\alpha^4 - 2\Delta f\alpha^2)$, where λ and C_s are the wavelength and spherical aberration coefficient, becomes the same and are given by

$$\gamma_g = -\pi/2\lambda(C_s\alpha_1^2\alpha_2^2). \qquad (1)$$

Therefore, 865 Å is the optimum defocus value to obtain the same phase for all 000, 200, 1$\bar{1}$1 and 11$\bar{1}$ waves at 100kV with tilted illumination. The corresponding contrast transfer function and the equal-phase zone at the back focal plane are shown in Figs. 2(a) and (b). The equal-phase zone ranges from 0·133 to 0·400 Å^{-1} which correspond to 7·518-2·500 Å. The information on the planes (111) and (200), whose spacings are 2·355 and 2·039 Å, is reproduced in the image plane as if their spacings are 2·890 and 4·081 Å. At this defocus, even structure in the image with a period of 1·25 Å can be recorded with the correct phase. This imaging method is useful for the study of the atomic structure around defects such as dislocations and stacking faults, because diffuse scattering and streaks in the diffraction pattern (which are caused by the small displacements of atoms around the defects) are projected onto the image plane without phase shift, and produce images of the displaced atoms in their correct position.
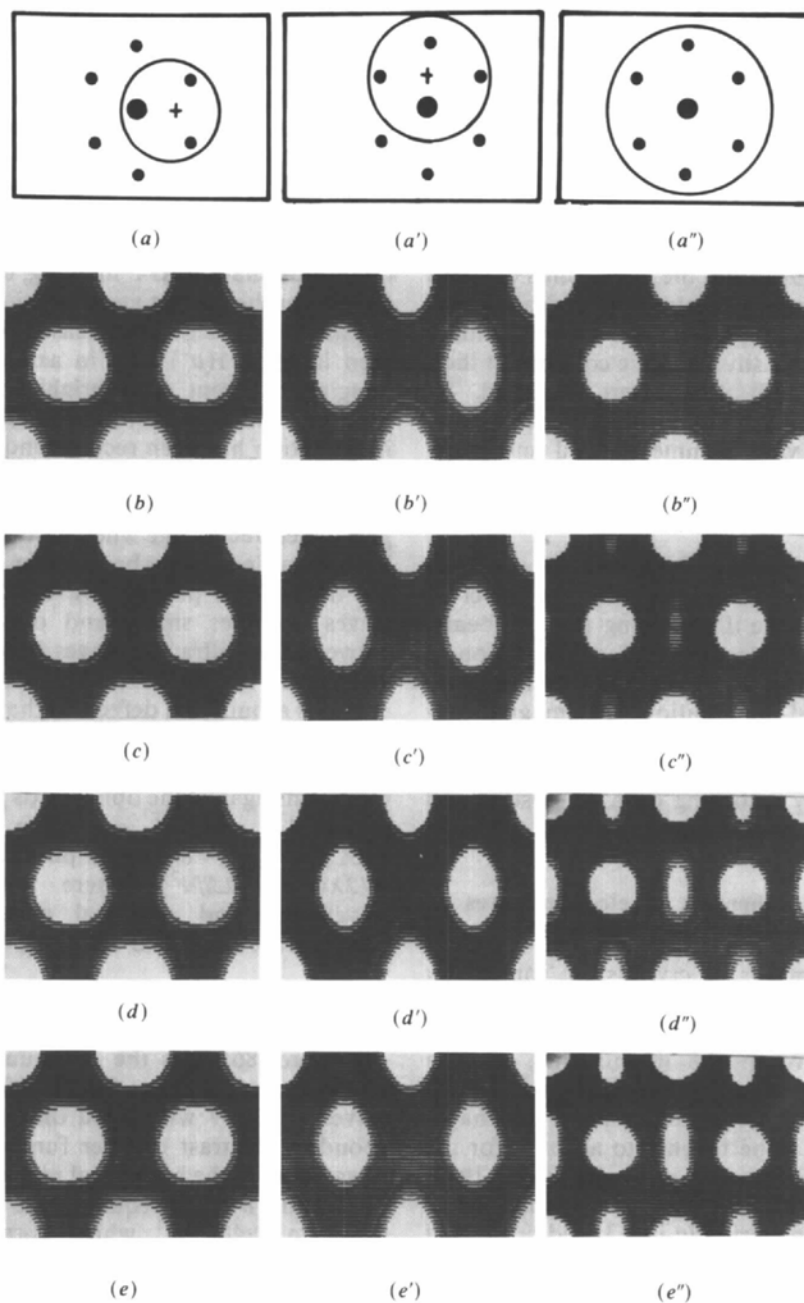
Fig. 1. Effect of partial coherence on the imaging condition. (a) and (a') are tilted-illumination AFF imaging, (a'') is axial-illumination AFF imaging. (b), (c), (d) and (e) are for ($\alpha_0 = 0$, $\Delta_0 = 0$), ($\alpha_0 = 0{\cdot}1$ mrad, $\Delta_0 = 50$ Å), ($\alpha_0 = 0{\cdot}3$ mrad, $\Delta_0 = 100$ Å) and ($\alpha_0 = 1$ mrad, $\Delta_0 = 200$ Å), respectively, where α_0 and Δ_0 are the beam divergence and chromatic defocus value. Circles in (a), (a') and (a'') indicate the aperture position shown in the diffraction patterns. Centers of circles are the projections of optical axes. Half-tone pictures are calculated images of unit cells of gold crystals in the [011] orientation (103·8 Å thickness). Defocus is 649, 865 and 2056 Å from left to right. $C_s = 0{\cdot}7$ mm, excited waves 129.

3. Specimen preparation and recording of the images of moving atoms

Specimens of thin gold crystals in the [011] orientation with a thickness of 100(20) Å were prepared by vacuum deposition on a single silver crystal. Details of specimen preparation are described in the previous paper (Takai, Hashimoto & Endoh, 1983).
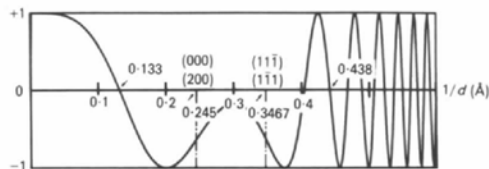
To record images of moving atoms, the current density of the illuminating electron beam on the specimen was 100–200 A cm⁻², and the images were magnified 1 300 000 times on the fluorescent screen of the electron microscope and projected onto the monitor screen by a TV camera, which is attached under the fluorescent screen with a magnification of 35 000 000 times. The electron beam intensity on the fluorescent screen was 6×10^{-11}–$1 \cdot 2 \times 10^{-10}$ A cm⁻² and the image size of atoms of 2 Å diameter becomes 7mm in diameter on the monitor screen. After recording every process of the moving atoms onto videotape, some processes were transferred to a movie film, and also to ordinary photographic film. Each frame of a TV image records the phenomena which take place during 1/30 s.

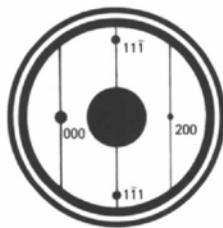## 4. Edge dislocation and its movement

Fig. 3 is an example of the image of a gold crystal containing the core of an edge dislocation in the center. As was discussed in § 3, white dots represent the positions of gold atoms in the crystal even near the core of a dislocation, where the displacement of atoms is predominant. By viewing obliquely from the

(a)

Fig. 2. (a) Real part of contrast transfer function for $\Delta f = 865$ Å, $C_s = 0 \cdot 7$ mm. (b) The equal-phase zone at the plane of the diffraction pattern (back focal plane). The lines passing across the diffraction spots represent the streaks due to a defect in (111), which reproduce the displaced atom position correctly at the image plane. (a) and (b) are at 100 kV with tilted illumination.

bottom right and bottom left of Fig. 3(a) the extra half atomic planes are clearly seen.

By drawing a Burgers circuit, it is easily seen that the Burgers vector is $\mathbf{b} = \mathbf{a}/2\,[0\bar{1}1]$. From the arrangement of white dots, it can be seen that there is an edge dislocation in the center, whose dislocation line
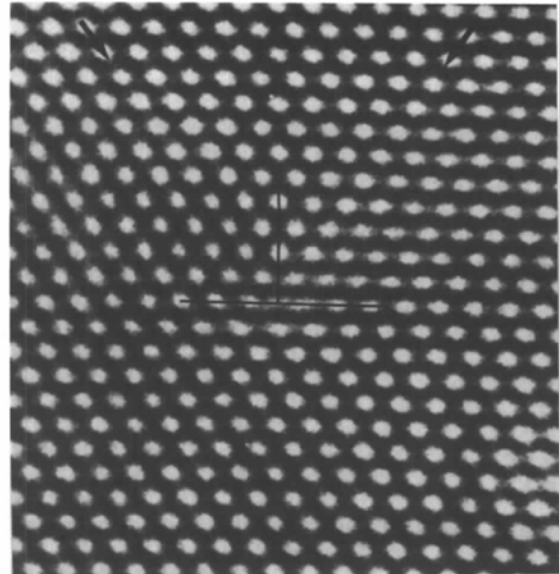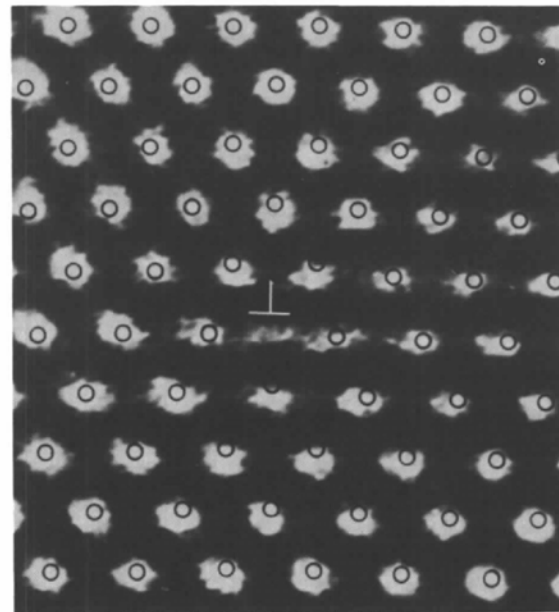

(a)

(b)

Fig. 3. (a) Images of an edge dislocation in a gold crystal in the [011] orientation. (b) High magnification of (a). White dots represent the images of gold atom columns in crystal. Black circles on white dots represent the positions of atom columns predicted by the theory of elasticity.

is perpendicular to the crystal surface. Fig. 3(b) is an enlargement of Fig. 3(a), and black circles are drawn on the white dots whose positions correspond to those calculated by the theory of elasticity. The agreement of the centers of the white dots and the black circles is good in a region separated by more than 0·6 nm from the core of the dislocation, but near the core of the dislocation they are separated by more than 0·02 nm. Though the atoms arranged on (100) are displaced by a comparatively large amount near the

core of the dislocation in the model proposed by the theory of elasticity, the observed white dots are arranged with rather small displacement, which is nearly the same as the atomic positions predicted by the theory considering interatomic potentials (Perrin, Englert & Bullough 1972). White dots close to the core of dislocations are comparatively diffuse, which might be due to a small bending of the dislocation line, or the atoms in the core of the dislocation might have no definite position and have fluctuations. Though the diffuse streaks in the diffraction pattern are included rather widely in the present imaging, it might not be enough to reveal the fine structure of the image of the distorted region. Since at the present stage there is still some small uncertainty in the imaging conditions, such as the spherical aberration coefficient, defocus, Bragg reflecting condition, crystal thickness and so on, the theoretical calculation cannot completely make clear the atomic arrangement at the core of the dislocation.

Movement of edge dislocations was noted during the observation. Most of them moved in the ⟨110⟩ direction on {111}. However, as shown in Fig. 4, which shows images reproduced from the TV frames with an interval of 0·7 s, the core of a dislocation migrates three atomic distances (0·4 nm) along (100) within 1·4 s. The migration was smooth and continuous. This unusual migration seems to be due to the effect of the small thickness of the film and the anomalous stress imposed on the specimen film, which is due to the accumulation of contamination and the elevation of specimen temperature caused by electron beam irradiation.

5. Screw dislocation and its movement

Since the Burgers vector of a screw dislocation is parallel to its dislocation line, no anomaly of atomic arrangement can be seen in a structure image which is projected in the direction parallel to the dislocation line. However, if a screw dislocation dissociates into two partial dislocations, whose Burgers vectors have components normal to the direction of the incident beam, the core of the dislocation will be able to be observed as the displacement of atoms corresponding to the partial dislocation.

Fig. 5(a) shows an image of the region which seems to contain a screw dislocation normal to the crystal surface whose Burgers vector is [01̄1̄]. As shown by arrows, there is slight stacking disorder in horizontal (11̄1) and large spacing of inclined (111̄), which cannot be expected from the perfect crystal. As can be seen in Figs. 6 and 7, this imperfect region can move in various directions. This behavior strongly suggests that this contrast is due to a screw dislocation. In Figs. 5(b) and (c), the arrangement of two neighboring atomic layers in (11̄1) is shown by black and white discs. Fig. 5(b) shows a projection of atoms along
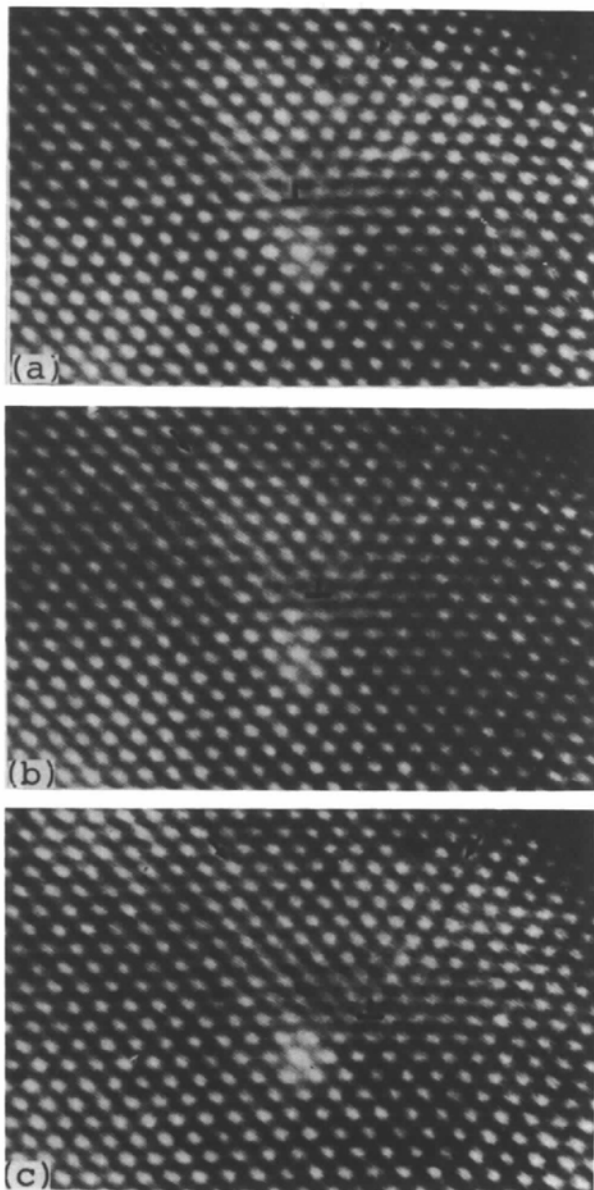

Fig. 4. Motion of an edge dislocation. Interval is 0·7 s. The central bright region is a defect of the TV screen and not related to atomic structure. The bending of the arrangement of white dots at the right top corner is due to the curvature of the TV monitor screen.

($1\bar{1}1$), which is normal to ($0\bar{1}\bar{1}$) shown in (a) and (c). It illustrates the displacement of atoms according to the following dissociation of a perfect dislocation $\mathbf{a}/2[0\bar{1}\bar{1}]$ into two partial dislocations:

$$\mathbf{a}/2[0\bar{1}\bar{1}] = \mathbf{a}/6[\bar{1}2\bar{1}] + \mathbf{a}/6[1\bar{1}\bar{2}]. \quad (2)$$

(a)

($1\bar{1}1$)

$\mathbf{a}/2[0\bar{1}\bar{1}] \longrightarrow \mathbf{a}/6[\bar{1}2\bar{1}] + \mathbf{a}/6[1\bar{1}\bar{2}]$

(b)
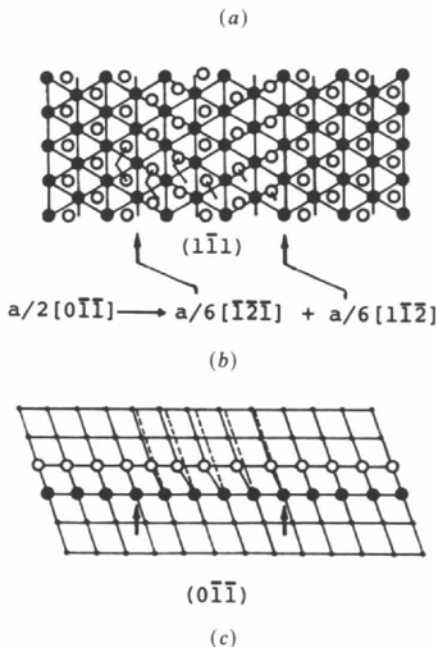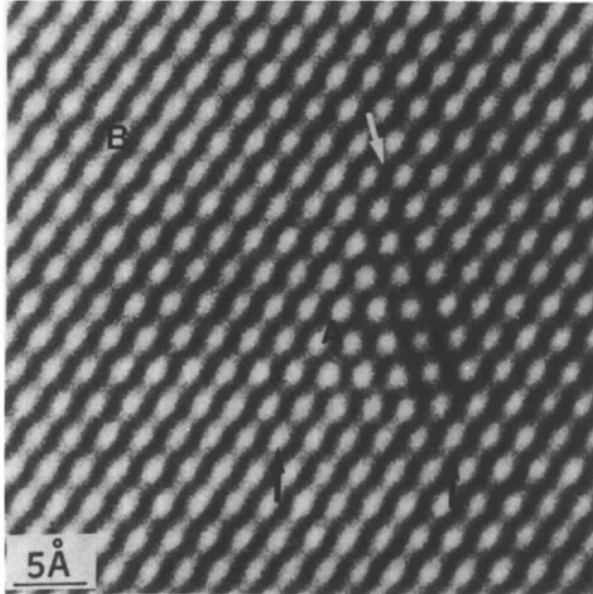

($0\bar{1}\bar{1}$)

(c)

Fig. 5. (a) Image of a gold crystal in the [011] orientation containing a possible screw dislocation. Arrows show the structure anomaly. Atom column images are clearly resolved at A and not at B, which is due to the change in the Bragg conditions. (b) Atom arrangement in ($1\bar{1}1$) showing the dissociation of a screw dislocation into two partial dislocations. (c) Atom arrangement projected onto ($0\bar{1}\bar{1}$). Black and white discs in (b) and (c) represent the atoms in neighboring ($1\bar{1}1$).

Fig. 5(c) is the projection of the displaced atoms shown in (b) onto ($0\bar{1}\bar{1}$), which is comparable to the image shown in (a). The agreement between (a) and (c) is fairly satisfactory. The observed width of the extended two partial dislocations is four to six atomic distances, which is rather small.

As can be seen in the regions indicated by A and B in Fig. 5(a), the atom column images are clearly resolved in A and not in B, which is due to a difference in the Bragg reflecting condition caused probably by Eshelby twist (Eshelby & Stroh, 1951; Tunstall, Hirsch & Steeds, 1964). The series of pictures in Fig. 6 show the motion of a screw dislocation extended. In these pictures a contrast region which is similar to the one shown in Fig. 5 is seen. It is seen that the dislocation moves four atoms distance (0.9 nm) during 0.4 s. Image contrast in (b) is diffuse compared with other figures (a), (c) and (d). This seems to be due to the movement of atoms accompanied by the movement of the dislocation during the recording.

Fig. 7 shows the movement of a screw dislocation normal to the slip plane ($11\bar{1}$). As illustrated at the right, one part of the extended dislocation with the contrast anomaly in ($1\bar{1}1$) is cross slipped and a contrast anomaly appears in ($11\bar{1}$) as seen in (b) and (c). These appear at positions separated by five atomic distances, within 1.2 s.

6. Mixed dislocation and its movement

Fig. 8 is an example of an image of the structure which is observed everywhere in the specimen. Since the images of atoms appear rather clearly, the dislocation line seems to be pependicular to the specimen surface. The Burgers vector is known to be $\mathbf{b}_1 = \mathbf{a}/2$ [110] or $\mathbf{b}_2 = \mathbf{a}/2[10\bar{1}]$ by drawing the Burgers circuit. Thus, this is a mixed dislocation. Though $\mathbf{b}_1$ and $\mathbf{b}_2$ make angles with the dislocation line of 120 and 60° respectively, their projections on the specimen surface parallel to ($0\bar{1}\bar{1}$) are the same, and thus it is assumed that the Burgers vector in the case of Fig. 8(a) is $\mathbf{b} = \mathbf{a}/2[10\bar{1}]$. This dislocation dissociates into two partial dislocations as given by the equation

$$\mathbf{a}/2[10\bar{1}] \rightarrow \mathbf{a}/6[21\bar{1}] + \mathbf{a}/6[1\bar{1}\bar{2}], \quad (3)$$

and contains an extrinsic stacking fault between them. The atomic arrangements of two atomic layers of ($1\bar{1}1$) and ($0\bar{1}\bar{1}$) are shown by black and white discs and are shown in Figs. 8(b) and (c) respectively. The Burgers vector of the partial dislocation on the left-hand side, $\mathbf{b}_l = \mathbf{a}/6[21\bar{1}]$, is at 90° to the dislocation line and the one on the right-hand side, $\mathbf{b}_r = \mathbf{a}/6[1\bar{1}\bar{2}]$, is at 30°; in total, they form a 60° dislocation of mixed character.

The atom positions near the stacking fault are displaced, especially in the first atom layer. A comparison of the observed atom positions and the calculated ones by the theory of elasticity has been carried
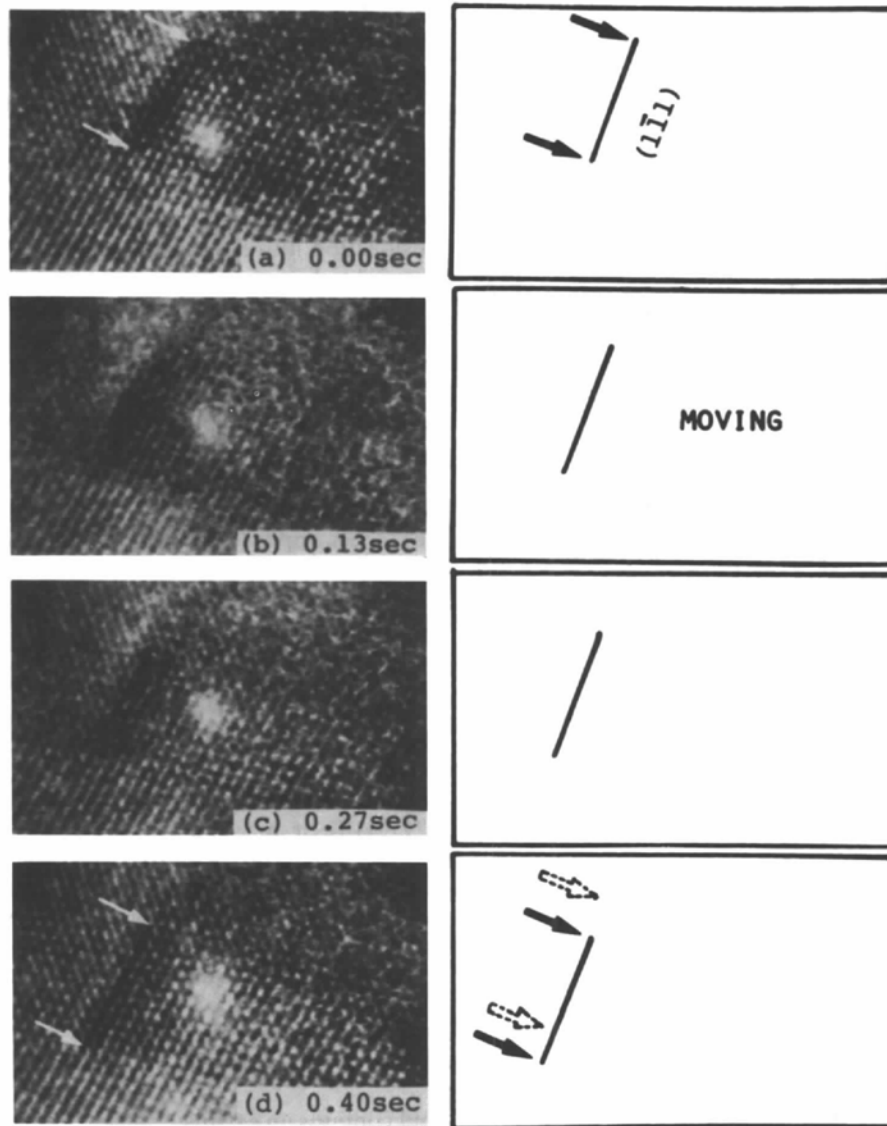
Fig. 6. Motion of an extended screw dislocation. Interval is 0·13 s.
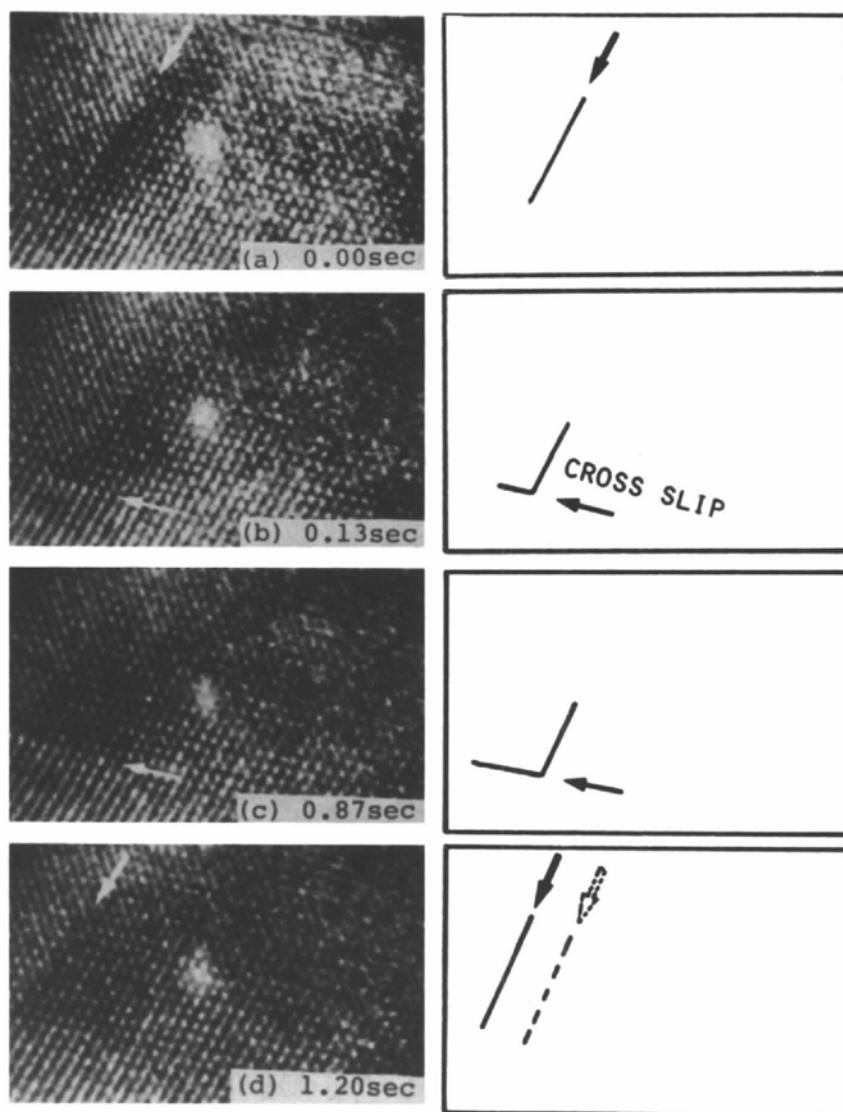
Fig. 7. Cross-slip motion of an extended screw dislocation. The frames are photographed at intervals of 0·13, 0·74, 0·33 s.

out and is shown in Fig. 9. In Fig. 9(a) small black dots represent the positions of the intensity maxima of the bright spot image and the small circles show the positions of atoms calculated by the theory of elasticity. Figs. 9(b) and (c) are plots of the displacement of atoms in the [21$\bar{1}$] direction. As can be seen in (b) and (c), calculated values are very different from the observed values in the first layer above the stacking-fault plane but no large difference is observed in the third layer. It must be emphasized here that the observed values are very similar to the calculated values from theory based on interatomic potentials.

The stacking-fault energy η can be calculated from the width of the partial dislocation, 1·7–2·2 nm, to be

$$\eta = 43\text{--}55 \times 10^{-3} \text{ J m}^{-2}$$

which is slightly larger than the well known value of 30×10^{-3} J m^{-2}, which seems to be due to the effect of the thickness of the specimen.

Fig. 10 shows the movement of a mixed dislocation and the deformation of the crystal. It can be seen in Fig. 10, with the slip movement of a partial dislocation b_1 along (111) in (a), that an intrinsic stacking fault is formed behind the partial dislocation b_1 as seen in (b). In (c), another partial dislocation b_2 moves up, and in (d) it goes out of sight leaving a deformation of one atomic distance remaining in the crystal. Velocity of migration of the partial dislocation b_2 is 20 nm s^{-1}.

(a)
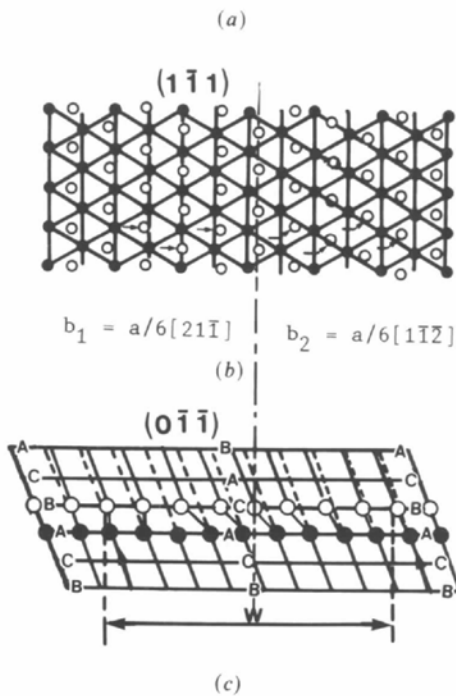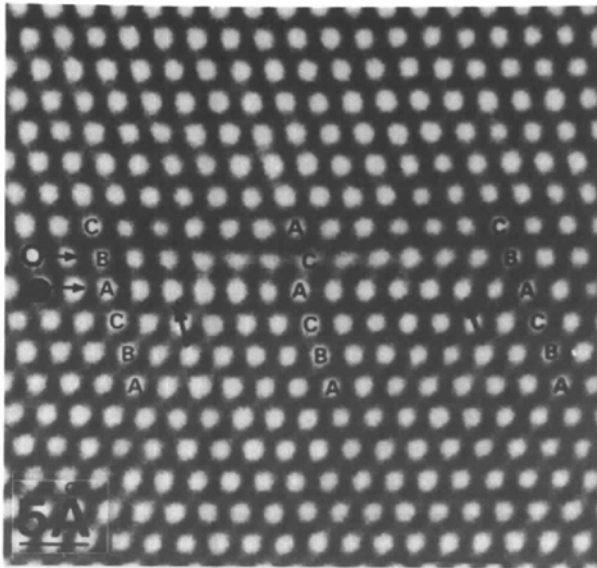

$b_1 = a/6[21\bar{1}]$ $b_2 = a/6[1\bar{1}\bar{2}]$

(b)

(0$\bar{1}\bar{1}$)

(c)

Fig. 8. (a) Image of a gold crystal containing an extended mixed dislocation. (b) Atom arrangement in (1$\bar{1}$1) showing the dissociation of a mixed dislocation into two partial dislocations containing a stacking fault between them. (c) Atom arrangement projected onto (0$\bar{1}\bar{1}$). Black and white discs in (b) and (c) represent the atoms in neighboring (1$\bar{1}$1).
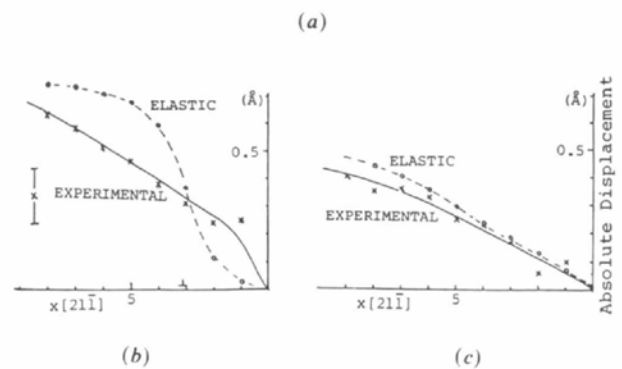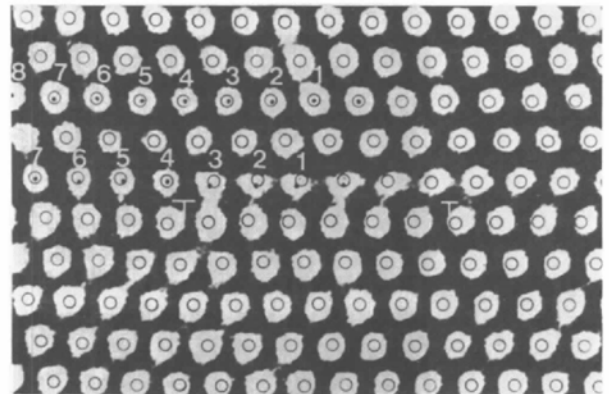

(a)

(b)   (c)

Fig. 9. (a) Comparison of the atom positions observed and calculated by the theory of elasticity. Circles show the positions of atoms according to the theory. Black dots represent the positions of intensity maxima of the image. Comparison of the measured and calculated displacements of atom positions in the first and the third layers in the direction of [21$\bar{1}$] are plotted in (b) and (c) respectively.
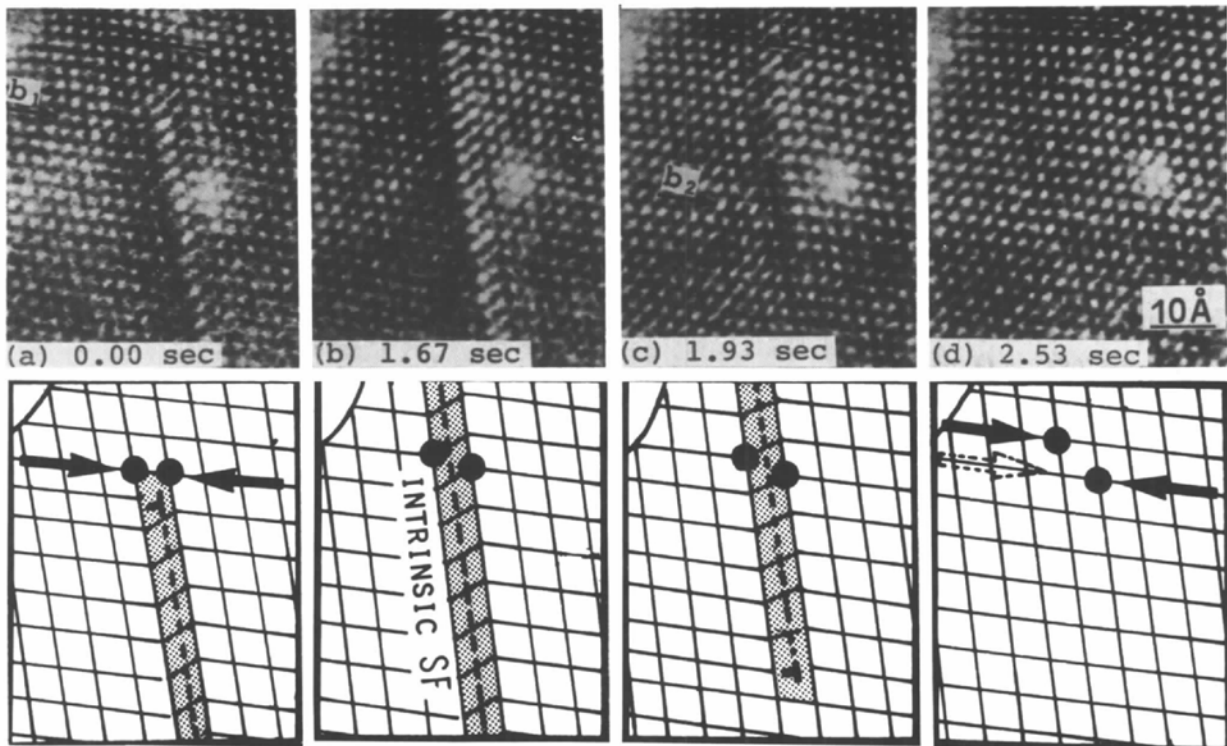
Fig. 10. Series of pictures showing the movement of atom columns due to the movement of a mixed dislocation. Note that the crystal is deformed one atomic distance after the movement of the dislocation. Intervals of the recording of the image are shown in the figures.

Slip motion of extended mixed dislocations like these was often observed.

References

BETHE, H. A. (1928). *Ann. Phys.* (*Leipzig*), **87**, 55–129.

BOVIN, J. O., WALLENBERG, R. & SMITH, D. J. (1985). *Nature* (*London*), **317**, 47–49.

CATTO, C. J. D., SMITH, K. C. A., NIXSON, W. C., ERASMUS, S. J. & SMITH, D. J. (1981). *Electron Microsc. Anal.* pp. 123–126.

COSSLETT, V. E. (1977). Proc. 5th Int. Conf. High Voltage Electron Microscopy, Kyoto, Japan, pp. 87–90.

COWLEY, J. M. & MOODIE, A. F. (1957). *Acta Cryst.* **10**, 609–619.

CREWE, A. V. (1978). Proc. 9th Int. Congr. Electron Microscopy, Toronto, Canada, Vol. 3, pp. 197–206.

ESHELBY, J. D. & STROH, A. N. (1951). *Philos. Mag.* **42**, 1401–1405.

HASHIMOTO, H. (1976). Analytical Electron Microscopy Workshop, Cornell Univ., Ithaca, NY, USA, pp. 74–79.

HASHIMOTO, H., ENDOH, H., TAKAI, Y., TOMIOKA, H. & YOKOTA, Y. (1978/79). *Chem. Scr.* **14**, 23–31.

HASHIMOTO, H., ENDOH, H., TAKAI, Y., YOKOTA, Y. & KUMAO, A. (1980). *Inst. Phys. Conf. Ser.* No. 52, pp. 3–8.

HASHIMOTO, H., KUMAO, A. & ENDOH, H. (1978). Proc. 9th Int. Congr. Electron Microscopy, Toronto, Canada, Vol. III, pp. 244–255.

HASHIMOTO, H., KUMAO, A., ETOH, T., FUJIWARA, K. & MAEDA, M. (1970). Proc. 7th Int. Congr. Electron Microscopy, Grenoble, France, Vol. II, pp. 461–462.

HASHIMOTO, H., SUGIMOTO, Y., TAKAI, Y. & ENDOH, H. (1978). Proc. 9th Int. Congr. Electron Microscopy, Toronto, Canada, Vol. 1, pp. 284–285.

HASHIMOTO, H. & TAKAI, Y. (1985). *J. Microsc.* (*Oxford*), **142**, 119–129.

HASHIMOTO, H., TAKAI, Y., YOKOTA, Y., ENDOH, H. & FUKADA, E. (1980). *Jpn. J. Appl. Phys.* **19**, L1–L4.

HASHIMOTO, H., TAKAI, Y., YOKOTA, Y., KUMAO, A., ENDOH, H., FUKADA, E. & TOMIOKA, H. (1979). *37th Annu. Proc. EMSA, Texas, USA*, pp. 384–387. Baton Rouge: Claitor.

HASHIMOTO, H., TANAKA, K., KOBAYASHI, K., SHIMAZU, S., NAIKI, T. & MANNAMI, M. (1958). Proc. 4th Int. Congr. Electron Microscopy, Berlin, Federal Republic of Germany, pp. 477–479.

HASHIMOTO, H., YOKOTA, Y., TAKAI, Y., ENDOH, H. & KUMAO, A. (1978/79). *Chem. Scr.* **14**, 125–128.

HOWIE, A. & WHELAN, M. J. (1961). *Proc. R. Soc. London Ser. A*, **263**, 217–237.

HOWIE, A. & WHELAN, M. J. (1962). *Proc. R. Soc. London Ser. A*, **267**, 206–230.

IIJIMA, S. & ICHIHASHI, T. (1985). *Jpn. J. Appl. Phys.* **24**, L125–L128.

IMURA, T., SAKA, H. & YUKAWA, T. (1970). *J. Electron Microsc.* **19**, 231–236.

ISAACSON, M. S. (1976). Proc. 6th Eur. Congr. Electron Microscopy, Jerusalem, Israel, Vol. 2, p. 26.

ISHIZUKA, K. (1980). *Ultramicroscopy*, **5**, 55–65.

MARKS, L. D. & SMITH, D. J. (1983). *Nature* (*London*), **303**, 316–317.

MIYAKE, S., FUJIWARA, K., TOKONAMI, M. & FUJIMOTO, F. (1964). *Jpn. J. Appl. Phys.* **3**, 276–285.

O'KEEFE, M. A. (1979). *37th Annu. Proc. EMSA*, Vol. 1, pp. 556–557. Baton Rouge: Claitor.

PERRIN, R. C., ENGLERT, A. & BULLOUGH, R. (1972). *Interatomic Potentials and Simulation of Defects*, edited by P. C. GEHEN, J. R. BELLER JR & R. I. JAFFEE, p. 509, New York: Plenum.

SINCLAIR, R., PONCE, F. A., YAMASHITA, T., SMITH, D. J., CAMPS, R. A., FREEMAN, L. A., ERASMUS, S. J., NIXSON, W. C., SMITH, K. C. A. & CATTO, C. J. D. (1982). *Nature (London)*, **298**, 127–131.

TAKAI, Y., HASHIMOTO, H. & ENDOH, H. (1983). *Acta Cryst.* **A39**, 516–522.

TAKAI, Y., HASHIMOTO, H., ENDOH, H. & AJIKA, N. (1981). *Proc. 61st EMAG Conf.*, Cambridge, England, pp. 361–364.

TUNSTALL, W. J., HIRSCH, P. B. & STEEDS, J. (1964). *Philos. Mag.* **9**, 99–119.

WHELAN, M. J., HIRSCH, P. B., HORN, R. W. & BOLLMANN, W. (1957). *Proc. R. Soc. London Ser. A*, **240**, 524–538.

Long-Period Structures in the Nb–Ga System

BY M. TAKEDA,* G. VAN TENDELOO AND S. AMELINCKX

University of Antwerp, RUCA, Groenenborgerlaan 171, B-2020 Antwerp, Belgium

Abstract

The alloys $NbGa_{3-x}$ form composition-driven long-period superstructures derived from the $D0_{22}$ by the introduction of non-conservative antiphase boundaries along (001) planes. The displacement vectors of successive antiphase boundaries are alternately $\frac{1}{4}$ [201] and $\frac{1}{4}$ [021]. In alloys with a composition which deviates less from $NbGa_3$ than Nb_5Ga_{13} successive antiphase boundaries all have the same displacement vector, either $\frac{1}{4}$ [201] or $\frac{1}{4}$ [021]. The alloy Nb_5Ga_{13} is the first material which has a long-period superstructure based on the alternation of two types of antiphase boundaries.

1. Introduction

In a recent paper (Takeda, Van Tendeloo & Amelinckx, 1987) we reported briefly on a redetermination of the structure of Nb_5Ga_{13}. It was found that this structure is tetragonal and has an unusually large c parameter of ~ 80 Å. The structure is a long-period antiphase-boundary modulated superstructure of the $D0_{22}$ structure. The superstructure is composition driven; the excess niobium as compared to the ideal composition $NbGa_3$ of the $D0_{22}$ structure is accommodated in this structure along non-conservative antiphase boundaries, belonging alternately to two different families. In the present paper we report more detailed results on Nb_5Ga_{13} as well as on the structures of alloys in the same binary system but with a slightly different composition.

---

* On leave from Toyohashi University of Technology, 1-1 Hibarigaoka, Tenpakucho, Toyohashi 440, Japan.

2. Preparation of materials and specimens

The alloys were prepared by alloying the elements in the appropriate proportions by dissolving niobium in molten gallium. The molten mixture was then quenched to room temperature and subsequently annealed at 1370 K, which is below the peritectic decomposition temperature of 1508 K, over 14 d. Specimens for electron microscopy and electron diffraction are prepared by crushing the brittle material. We prepared and examined alloys with a nominal composition in the range between Nb_4Ga_{10} and $NbGa_3$.

3. Crystallographic considerations; structural building principle

The structure of Nb_5Ga_{13} was determined by Schubert (1964). It was found to be a long-period out-of-phase boundary modulated superstructure derived from the deformed $D0_{22}$ structure of $NbGa_3$, which is itself a superstructure derived from a face-centred-based $L1_2$ structure. The $D0_2$ structure is derived from the $L1_2$ structure by the introduction of periodic *conservative* antiphase boundaries. On the other hand the Nb_5Ga_{13} structure is derived from the $D0_{22}$ structure by the introduction of *non-conservative* out-of-phase boundaries after every two $D0_{22}$ unit cells. In the model of Schubert (Fig. 1b) all the out-of-phase boundaries have the same displacement vector; we shall show that the essential features of the model are correct, but that the out-of-phase boundaries have alternately two different displacement vectors, which are related by the tetragonal symmetry of the $D0_{22}$ basic structure (Figs. 1a,c). As a result the long period

---